

# Scattering by two-dimensional rough surfaces: comparison between the method of moments, Kirchhoff and small-slope approximations

Gabriel Soriano, Charles-Antoine Guérin and Marc Saillard

Institut Fresnel, UMR CNRS 6133, Faculté des Sciences de Saint-Jérôme, case 162, F-13397 Marseille cedex 20, France

E-mail: charles-antoine.guerin@fresnel.fr

Received 12 July 2001, in final form 20 September 2001

Published 2 November 2001

Online at [stacks.iop.org/WRM/12/63](http://stacks.iop.org/WRM/12/63)

## Abstract

We use a rigorous numerical code based on the method of moments to test the accuracy and validity domains of two popular first-order approximations, namely the Kirchhoff and the small-slope approximation (SSA), in the case of two-dimensional rough surfaces. The experiment is performed on two representative types of surfaces: surfaces with Gaussian spectrum, which are the paradigm of single-scale surfaces, and ocean-like surfaces, which belong to the family of multi-scale surfaces. The main outcome of these computations in the former case is that the SSA is outperformed by the Kirchhoff approximation (KA) outside the near-perturbative domain and in fact is quite unpredictable in that its accuracy does not depend only on the slope. For ocean-like surfaces, however, SSA behaves surprisingly well and is more accurate than the KA.

(Some figures in this article are in colour only in the electronic version)

## 1. Introduction

An important issue in remote sensing applications is to interpret the electromagnetic field scattered by a dielectric or conducting two-dimensional rough surface. A typical configuration is a satellite illuminating the sea surface or agricultural soils with monochromatic waves at  $20^\circ$  of incidence. A sensibility of the backscattering coefficient to parameters such as wind speed over the sea and ocean salinity or soil moisture has been observed in experimental data and is also predicted by theoretical models. However, for a retrieval procedure of these parameters, a good modelling of the surfaces together with a reliable computation of the scattered field is needed.

The rigorous computation of scattering by 2D surfaces has recently been made possible by the drastic improvement of computer capacities combined with efficient numerical methods.

However, it still remains highly time-demanding and dissuasive when it comes to large surfaces or Monte Carlo simulations. In that case, first-order approximate methods such as the first-order Kirchhoff approximation (KA) or the small-slope approximation (SSA) are of great interest, provided, of course, that they can be relied on in the given regime of frequency. The domain of validity of such methods has been clearly established in the 1D case for single-scale surfaces and more recently for ocean-like spectra through numerical investigations (see, for example, [1] for a review on the KA and [2, 3] for the SSA).

An important step yet to be taken is to investigate the 2D case in view of the processing of natural surfaces. For ocean-like surfaces, some numerical results using the method of moments (MoM) have already been performed [4] in order to test the two-scale model based on the KA and the small perturbation method (SPM). This gives some indication of the choice of the cutoff frequency separating the small and large scales. However, this cutoff occurs in a domain where the accuracy of neither the KA nor the SPM is guaranteed. This makes alternative methods such as the SSA interesting since the latter is designed to make a continuous transition between the SPM and the KA. The SSA has been introduced quite recently [5, 6] and to our knowledge has not been systematically tested in the 2D case.

In this paper, we make a numerical comparison between the MoM and both the KA and the SSA, in a domain where the SPM is not applicable. As for any numerical study, only a small number of parameters can be taken into account. We have chosen to treat two generic cases of random rough surfaces: surfaces with Gaussian correlation, that can be considered as the prototype of single-scale (i.e. smooth) surfaces, and surfaces with power-law spectra, which are typical for multi-scale (i.e. fractal) surfaces such as ocean surfaces. The height distribution is assumed to be Gaussian and we deal only with perfectly conducting surfaces, the dielectric case being left for subsequent work. Furthermore, the incidence has been fixed to  $20^\circ$ , which is a typical satellite remote sensing configuration. Our numerical study relies on a comparison of the scattering diagrams in the main incidence plane for both polarization cases, with particular attention given to the backscattering cross section. We aim to establish empirical criteria that ensure the accuracy of either method, to avoid heavy and unnecessarily rigorous computations. We have systematically computed the energy balance to see whether it can be used as an *a priori* accuracy criterion.

The paper is organized as follows. Section 2 presents the scattering problem, and section 3 deals with the approximate methods. The MoM is introduced in section 4 and the numerical results are discussed in section 5.

## 2. The scattering problem

### 2.1. Definitions and notations

We follow closely the presentation and notation of Voronovich [7] for the scattering amplitude and its different approximations. A rough surface  $\Sigma$  separates the vacuum (upper medium) from an infinitely conducting medium (lower medium). We chose the right Cartesian coordinate  $(\hat{x}, \hat{y}, \hat{z})$  system with  $z$ -axis directed upward and assume  $\Sigma$  is given by an Cartesian equation  $z = h(\mathbf{r}) = h(x, y)$ . An electromagnetic plane wave with wavevector  $\mathbf{K}_0$  is incident down on to the surface, giving rise after reflection to outgoing plane waves  $\mathbf{K}$  in all directions of the upper half-space. (Some authors choose to place the vacuum in the lower medium and to illuminate the surface from below; this amounts to changing  $q \rightarrow -q$  in all subsequent formulae.) We denote the horizontal and vertical components of the wave vector by  $\mathbf{k}$  and  $\mathbf{q}$ , respectively. They satisfy the relation  $k_0^2 + q_0^2 = k^2 + q^2 = K^2 = K_0^2$ . Here and everywhere the null subscript refers to the incident field, as opposed to the scattered field; for an arbitrary

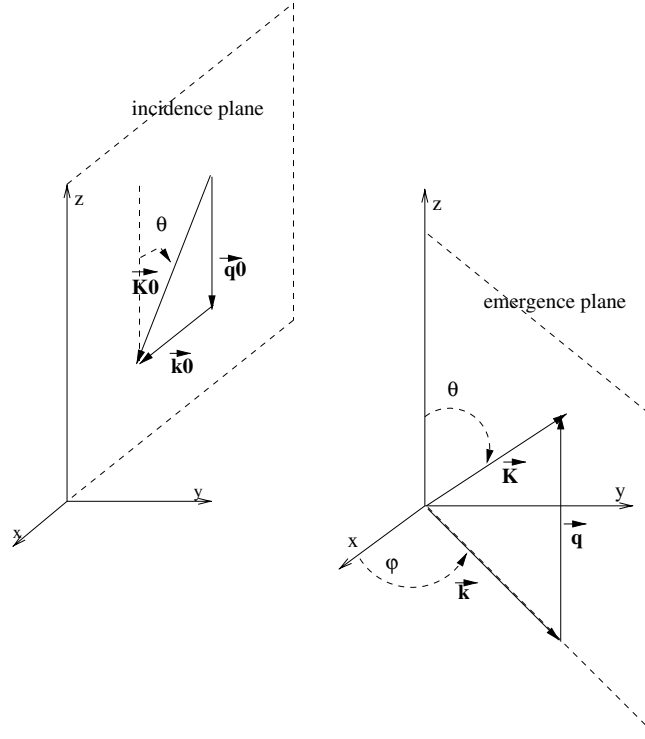


Figure 1. Geometry of the scattering problem.

vector  $\mathbf{a}$ , the notation  $a$  refers to its norm and  $\hat{\mathbf{a}}$  to its direction. The direction of propagation is characterized by a polar angle  $\theta = (\hat{\mathbf{z}}, \hat{\mathbf{K}})$  and an azimuthal angle  $\varphi = (\hat{\mathbf{x}}, \hat{\mathbf{k}})$ . The geometry of the problem is depicted in figure 1. The incidence plane is fixed to the  $(\hat{\mathbf{x}}, \hat{\mathbf{z}})$  plane, that is  $\varphi_0 = 0$ .

The electromagnetic field  $(\mathbf{E}, \mathbf{H})$  can be decomposed over the fundamental cases of polarization:

$$\begin{aligned} \mathbf{E}_\alpha &= q^{-1/2} \exp(i\mathbf{k} \cdot \mathbf{r} + \mathbf{q} \cdot \mathbf{z}) \mathbf{p}_\alpha(\mathbf{k}), & \alpha &= 1, 2 \\ \mathbf{H}_\alpha &= Z_0 \hat{\mathbf{K}} \times \mathbf{E}_\alpha \end{aligned}$$

where  $Z_0 = \sqrt{\mu_0/\epsilon_0}$  is the vacuum impedance and  $\mathbf{p}_\alpha$  is the polarization, with

$$\begin{aligned} \mathbf{p}_1(\mathbf{k}) &= \frac{k\hat{\mathbf{z}} - \mathbf{q} \cdot \hat{\mathbf{z}}\hat{\mathbf{k}}}{K} \\ \mathbf{p}_2(\mathbf{k}) &= \hat{\mathbf{z}} \times \hat{\mathbf{k}}. \end{aligned}$$

The case  $\alpha = 1$  corresponds to vertical polarization (V-polarization), where the electric field lies in the  $(\hat{\mathbf{z}}, \hat{\mathbf{k}})$  plane;  $\alpha = 2$  is the horizontal polarization (H-polarization), with an electric field in the horizontal plane  $(\hat{\mathbf{x}}, \hat{\mathbf{y}})$ . The normalization factor  $q^{-1/2}$  is chosen to obtain a constant ( $= Z_0/K$ ) Poynting vector flow through a horizontal unit surface. An implicit harmonic time dependence  $e^{-i\omega t}$  is always assumed.

The scattering amplitude describes the response of the surface to a plane wave in a given direction of space and polarization. Precisely, for an  $\alpha$ -polarized incident electric field  $\mathbf{E}_\alpha^0$ ,

the  $\beta$ -polarized component of the scattered field can be expressed as

$$\mathbf{E}_\beta = \int d\mathbf{k} S_{\beta\alpha}(\mathbf{k}, \mathbf{k}_0) q^{-1/2} \exp(i\mathbf{k} \cdot \mathbf{r} + iqz) \mathbf{p}_\beta(\mathbf{k}).$$

The two-by-two matrix  $S(\mathbf{k}, \mathbf{k}_0) = (S_{\beta\alpha}(\mathbf{k}, \mathbf{k}_0))$  is called the scattering matrix. Note that the integral runs over  $\mathbb{R}^2$ . The components with  $k \leq K$  correspond to propagating waves while  $k > K$  (and  $q = i\sqrt{(k^2 - K^2)}$ ) corresponds to evanescent waves.

## 2.2. Finite beams

The scattering amplitude is defined for incident plane waves. However, most rigorous numerical methods make use of tapered (usually Gaussian) incident fields, to limit the size of the surface that participates in the scattering process [8–10]. A purely V- or H-polarized convergent beam  $\mathbf{E}_\alpha^0$  can be obtained in the form

$$\mathbf{E}_\alpha^0 = \int_{k_0 \leq K} d\mathbf{k}_0 \tilde{g}(\mathbf{k}_0 - \bar{\mathbf{k}}_0) \exp(i\mathbf{k}_0 \cdot \mathbf{r} - q_0 z) \mathbf{p}_\alpha(\mathbf{k}_0), \quad (2.1)$$

where the Gaussian  $\tilde{g}$  is the spectral amplitude function:

$$\tilde{g}(\mathbf{k}) = \sqrt{\frac{\ell_x \ell_y}{\pi}} \exp\left(-\frac{1}{2}(\ell_x^2 k_x^2 + \ell_y^2 k_y^2)\right), \quad (2.2)$$

and the notation  $\tilde{g}$  stands for the Fourier transform of a function  $g$ :

$$\tilde{g}(\mathbf{k}) = \int e^{-i\mathbf{k} \cdot \mathbf{r}} g(\mathbf{r}) d\mathbf{r}.$$

The characteristic size of the illuminated patch on the surface is then  $\ell_x, \ell_y$ . Summing all the contributions of the plane waves forming the incident field, the  $\beta$ -polarized component of the scattered field is obtained as

$$\mathbf{E}_\beta = \int d\mathbf{k} \bar{S}_{\beta\alpha}(\mathbf{k}, \bar{\mathbf{k}}_0) q^{-1/2} \exp(i\mathbf{k} \cdot \mathbf{r} + qz) \mathbf{p}_\beta(\mathbf{k}), \quad (2.3)$$

with

$$\bar{S}_{\beta\alpha}(\mathbf{k}, \bar{\mathbf{k}}_0) = \int_{k_0 \leq K} d\mathbf{k}_0 q_0^{1/2} \tilde{g}(\mathbf{k}_0 - \bar{\mathbf{k}}_0) S_{\beta\alpha}(\mathbf{k}, \mathbf{k}_0). \quad (2.4)$$

The quantity  $\bar{S}_{\beta\alpha}(\mathbf{k}, \bar{\mathbf{k}}_0)$  is the scattering amplitude in outgoing direction  $\mathbf{k}$  for a finite beam with mean incident direction  $\bar{\mathbf{k}}_0$ .

Since the polarization vector  $\mathbf{p}_\alpha$  varies with the wavevector, the amplitude of the incident field on the surface mean plane is not Gaussian. This is a typical artefact of vector wave scattering [11] that does not exist in the 1D case or the scalar 2D case. This is particularly visible at near-normal incidence, where a pronounced minimum appears at the centre of the spot (see figure 2). To circumvent this problem we use a more adapted basis of polarization vectors, namely

$$\begin{aligned} \mathbf{p}_E(\mathbf{k}) &= \frac{-\cos \varphi \mathbf{p}_1 + \cos \theta \sin \varphi \mathbf{p}_2}{\sqrt{\sin^2 \varphi \cos^2 \theta + \cos^2 \varphi}} = \frac{\mathbf{k} \times \hat{\mathbf{y}}}{\|\mathbf{k} \times \hat{\mathbf{y}}\|} \\ \mathbf{p}_H(\mathbf{k}) &= \frac{-\sin \varphi \cos \theta \mathbf{p}_1 - \cos \varphi \mathbf{p}_2}{\sqrt{\sin^2 \varphi \cos^2 \theta + \cos^2 \varphi}} = \hat{\mathbf{K}} \times \mathbf{p}_E(\mathbf{k}). \end{aligned}$$

Correspondingly, the incident field assumes the form (2.1), with  $\mathbf{p}_\alpha$  replaced by  $\mathbf{p}_E(\mathbf{k})$  or  $\mathbf{p}_H(\mathbf{k})$ . The polarization vector  $\mathbf{p}_E(\mathbf{k})$  now remains perpendicular to the main incidence plane ( $\hat{\mathbf{x}}, \hat{\mathbf{z}}$ ), which limits the destructive interference within the beam. Figure 2 indeed shows

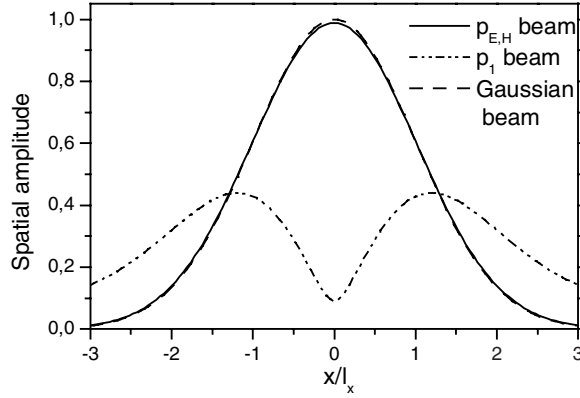


Figure 2. Effect of the polarization basis on the amplitude of the incident field in the spatial domain.

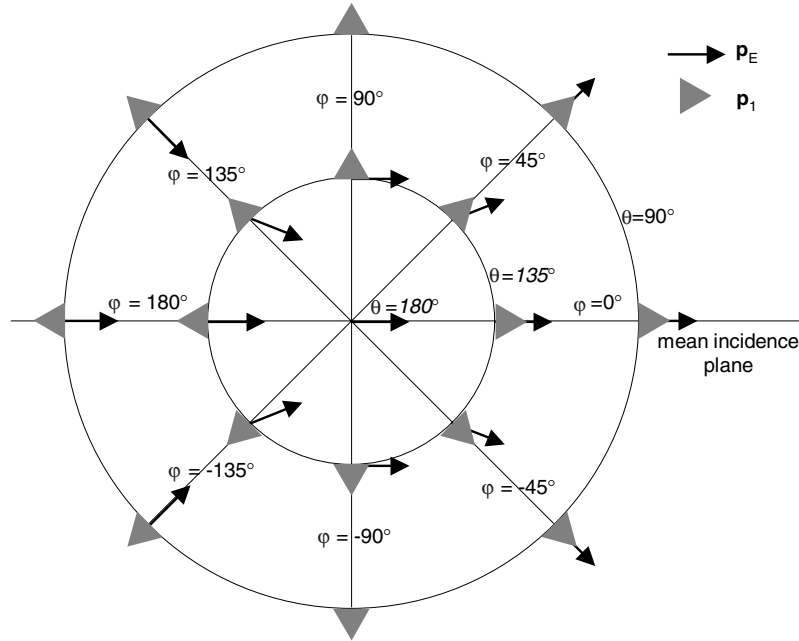


Figure 3. Comparison between the different polarization bases at different angles.

that deviation from Gaussianity is considerably reduced. Note that  $p_E$  coincides with the V-polarization  $p_1$  in the mean incidence plane. In the same way,  $p_H(\mathbf{k})$  corresponds the H-polarization  $p_2$  in the mean incidence plane. A comparison between polarizations  $p_1$  and  $p_E$  is shown in figure 3. As soon as  $\bar{k}_0 \gg 1/\ell_x$ , that is away from the normal incidence, there is no perceptible deviation to Gaussianity for any basis of polarization.

For the beam widths and the mean incidence angle used in this work ( $\ell_x = \ell_y = 4\lambda$ ,  $\bar{\theta}_0 = 20^\circ$ ), we have verified that building the incident field with one polarization basis or the other has no influence on the co-polarized scattered field in the mean incidence plane for mildly rough surfaces.

### 2.3. Scattered power

The total scattered power  $\Phi$  can be defined as the flux of the complex Poynting vector through a horizontal plane  $z = z_m$  above the surface (i.e.  $z_m > \max(h)$ ):

$$\Phi = \text{Re} \int_{z=z_m} \frac{1}{2} \mathbf{E} \times \mathbf{H}^* \cdot \hat{\mathbf{z}} \, dx \, dy.$$

Likewise, the total incident power is the flux of the incident Poynting vector

$$\Phi_0 = -\text{Re} \int_{z=z_m} \frac{1}{2} \mathbf{E}^0 \times \mathbf{H}^{0*} \cdot \hat{\mathbf{z}} \, dx \, dy.$$

For fixed  $z$ , the incident as well as scattered fields can be seen as Fourier transforms in the  $\mathbf{k}$ -domain. Using Parseval's formula, this leads to integrals in the spectral domain for the incident and scattered power:

$$\begin{aligned} \Phi_0 &= \frac{Z_0}{2K} \int_{k \leq K} d\mathbf{k} \, q \, |\tilde{g}(\mathbf{k})|^2, \\ \Phi &= \frac{Z_0}{2K} \sum_{\beta=1,2} \int_{k \leq K} d\mathbf{k} \, |\bar{S}_{\beta\alpha}(\mathbf{k}, \bar{\mathbf{k}}_0)|^2. \end{aligned}$$

Note that the incident flux becomes constant,  $\Phi_0 \rightarrow q_0$  as the beam becomes larger. The conservation of energy reads  $\Phi = \Phi_0$ . The outgoing flux will be normalized by the incident flux. Introducing  $d\Omega = \sin\theta \, d\theta \, d\phi$ , the solid angle element in direction  $\mathbf{K}$ , we have  $d\mathbf{k} = Kq \, d\Omega$  and thus we may define the scattered intensity as the scattered power per solid angle per unit incident power:

$$I_{\beta\alpha}(\mathbf{k}, \bar{\mathbf{k}}_0) = \frac{1}{\Phi_0} Kq \, |\bar{S}_{\beta\alpha}(\mathbf{k}, \bar{\mathbf{k}}_0)|^2.$$

The conservation of energy then reads

$$\int \sum_{\beta=1,2} I_{\beta\alpha}(\mathbf{k}, \bar{\mathbf{k}}_0) \, d\Omega = 1. \quad (2.5)$$

Note that other related quantities are also used in the remote sensing literature: the scattering cross section  $4\pi \cos\bar{\theta}_0 I_{\beta\alpha}$  and the scattering bistatic coefficient  $4\pi I_{\beta\alpha}$ .

## 3. The Kirchhoff and small-slope approximations

### 3.1. KA and SSA for plane waves

One of the most popular approximations in scattering from rough surfaces is the KA, also known as the tangent plane or physical optics approximation. It is known to be valid when the incident wavelength is small compared with the correlation length of the surface. The SSA, first introduced in [5], starts from a structure ansatz based on the invariance properties of the scattering amplitude. Performing a horizontal or vertical translation  $\mathbf{d}$  on the surface only affects the latter by a phase shift  $\exp(-i(\mathbf{k} - \mathbf{k}_0) \cdot \mathbf{d})$  or  $\exp(-i(\mathbf{q} + \mathbf{q}_0) \cdot \mathbf{d})$ , respectively, so that a solution is sought in the form

$$S(\mathbf{k}, \mathbf{k}_0) = \frac{1}{(2\pi)^2} \int d\mathbf{r} \exp(-i(\mathbf{k} - \mathbf{k}_0) \cdot \mathbf{d} - i(\mathbf{q} + \mathbf{q}_0)h(\mathbf{r})) \Xi[\mathbf{k}, \mathbf{k}_0, \mathbf{r}, h],$$

where  $\Xi$  is some functional that contains the explicit dependence on the surface ( $\Xi = 1$  for the plane). The unknown  $\Xi$  is obtained by performing a functional Taylor expansion with respect to the Fourier transform  $\tilde{h}$  and imposing the coefficients to be consistent with the SPM

as  $h \rightarrow 0$ . The first-order approximation for the KA and the SSA can be summarized in the following formula [7, pp 123 and 154]:

$$S(\mathbf{k}, \mathbf{k}_0) = B(\mathbf{k}, \mathbf{k}_0) \frac{2(qq_0)^{1/2}}{q + q_0} \frac{1}{(2\pi)^2} \int d\mathbf{r} \exp(-i(\mathbf{k} - \mathbf{k}_0) \cdot \mathbf{r} - i(q + q_0)h(\mathbf{r})), \quad (3.6)$$

where the matrix  $B(\mathbf{k}, \mathbf{k}_0)$  is given by

$$B(\mathbf{k}, \mathbf{k}_0) = \frac{1}{2qq_0} \begin{bmatrix} (K^2 + qq_0)\hat{\mathbf{k}} \cdot \hat{\mathbf{k}}_0 - kk_0 & K(q + q_0)\hat{\mathbf{z}} \cdot \hat{\mathbf{k}} \times \hat{\mathbf{k}}_0 \\ K(q + q_0)\hat{\mathbf{z}} \cdot \hat{\mathbf{k}} \times \hat{\mathbf{k}}_0 & -(K^2 + qq_0)\hat{\mathbf{k}} \cdot \hat{\mathbf{k}}_0 + kk_0 \end{bmatrix} \quad (3.7)$$

for the KA and

$$B(\mathbf{k}, \mathbf{k}_0) = \frac{1}{qq_0} \begin{bmatrix} K^2\hat{\mathbf{k}} \cdot \hat{\mathbf{k}}_0 - kk_0 & Kq_0\hat{\mathbf{z}} \cdot \hat{\mathbf{k}} \times \hat{\mathbf{k}}_0 \\ Kq\hat{\mathbf{z}} \cdot \hat{\mathbf{k}} \times \hat{\mathbf{k}}_0 & -qq_0\hat{\mathbf{k}} \cdot \hat{\mathbf{k}}_0 \end{bmatrix} \quad (3.8)$$

for the SSA. Note that the KA and SSA at first order differ only by the geometrical factor  $B(\mathbf{k}, \mathbf{k}_0)$ , which does not depend on the roughness. The off-diagonal terms of the scattering matrix vanish when  $\hat{\mathbf{k}} = \hat{\mathbf{k}}_0$ , meaning that no depolarization occurs in the incidence plane. In the specular direction ( $\mathbf{k} = \mathbf{k}_0$ ), the upper and lower diagonal elements for both approximations reduce to +1 and -1, respectively. In the limit  $h \rightarrow 0$ , the complex exponential in the integrand can be linearized, yielding

$$S(\mathbf{k}, \mathbf{k}_0) = B(\mathbf{k}_0, \mathbf{k}_0)\delta(\mathbf{k} - \mathbf{k}_0) - 2i(qq_0)^{1/2}B(\mathbf{k}, \mathbf{k}_0)\frac{1}{(2\pi)^2} \times \int d\mathbf{r} \exp(-i(\mathbf{k} - \mathbf{k}_0) \cdot \mathbf{r} - i(q + q_0)h(\mathbf{r})), \quad (3.9)$$

which is the classical formula of SPM when  $B(\mathbf{k}, \mathbf{k}_0)$  is given by (3.8).

### 3.2. KA and SSA for finite beams

The computation of the scattering amplitude  $\bar{S}_{\beta\alpha}$  in the KA or SSA after (2.4) and (3.6) involves a double summation over the space and frequency variable  $\mathbf{r}$  and  $\mathbf{k}_0$ , respectively, which becomes computationally demanding in the 3D case. However, the computation can be greatly simplified by assuming that the finite beam is sufficiently narrow (spectrally), so that we may approximate  $B(\mathbf{k}, \mathbf{k}_0) \simeq B(\mathbf{k}, \bar{\mathbf{k}}_0)$  and  $q_0 \simeq \bar{q}_0$  within the beam and extend the  $\mathbf{k}_0$  domain of integration to infinity. In that case, the integral over  $\mathbf{k}_0$  is a mere inverse Fourier transform of the beam envelope  $\bar{g}$ , which leads to

$$\bar{S}(\mathbf{k}, \bar{\mathbf{k}}_0) = B(\mathbf{k}, \bar{\mathbf{k}}_0) \frac{2q^{1/2}\bar{q}_0}{q + \bar{q}_0} \int d\mathbf{r} g(\mathbf{r}) \exp(-i(\mathbf{k} - \bar{\mathbf{k}}_0) \cdot \mathbf{r} - iq(+\bar{q}_0)h(\mathbf{r})). \quad (3.10)$$

This expression becomes accurate as the wavelength becomes small compared with the beam size,  $\lambda \ll l_x, l_y$ , or equivalently as the wavenumber becomes much larger than the spectral width,  $K \gg 1/l_x, 1/l_y$ .

### 3.3. Statistical approach

Most of the statistical results presented in this section are well known, but we revisit them with a different approach. A complete review of the statistical properties of the scattering amplitude in the KA can be found in [1]. Let the brackets  $\langle \cdot \rangle$  denote the ensemble average of some random quantity. Then we have

$$\langle I_{\beta\alpha}(\mathbf{k}, \bar{\mathbf{k}}_0) \rangle = \Phi_0^{-1} A_{\beta\alpha}(\mathbf{k}, \bar{\mathbf{k}}_0) \int d\mathbf{r} d\mathbf{r}' g(\mathbf{r})g(\mathbf{r}') \times \exp(-i(\mathbf{k} - \bar{\mathbf{k}}_0) \cdot (\mathbf{r} - \mathbf{r}'))L(q + \bar{q}_0; \mathbf{r}, \mathbf{r}'),$$

with

$$A_{\beta\alpha}(\mathbf{k}, \bar{\mathbf{k}}_0) = K \left| \frac{2q\bar{q}_0}{q + \bar{q}_0} \right|^2 |B_{\beta\alpha}(\mathbf{k}, \bar{\mathbf{k}}_0)|^2$$

and

$$L(q; \mathbf{r}, \mathbf{r}') = \langle \exp(-iq(h(\mathbf{r}) - h(\mathbf{r}')))) \rangle.$$

The function  $L(q; \mathbf{r}, \mathbf{r}')$  can be expressed in terms of second-order properties of the surface. If  $h(\mathbf{r})$  is a stationary Gaussian process with covariance function  $C(\mathbf{r})$ , then

$$L(q; \mathbf{r}, \mathbf{r}') =: L(q; \mathbf{r} - \mathbf{r}') = \exp(-q^2(C(0) - C(\mathbf{r} - \mathbf{r}'))).$$

Noting that the Fourier transform of  $L(q; \mathbf{r} - \mathbf{r}')$  is localized along the diagonal and using the convolution theorem we obtain

$$\langle I_{\beta\alpha}(\mathbf{k}, \bar{\mathbf{k}}_0) \rangle = \Phi_0^{-1} A_{\beta\alpha}(\mathbf{k}, \bar{\mathbf{k}}_0) \frac{1}{(2\pi)^2} \int d\mathbf{k}' |\tilde{g}_\alpha(\mathbf{k} - \bar{\mathbf{k}}_0 - \mathbf{k}')|^2 \tilde{L}(q + \bar{q}_0; \mathbf{k}').$$

For large beams we have  $|\tilde{g}_\alpha(\mathbf{k})|^2 \rightarrow \delta(\mathbf{k})$  and  $\Phi_0 = \bar{q}_0$ , yielding

$$\langle I_{\beta\alpha}(\mathbf{k}, \bar{\mathbf{k}}_0) \rangle = A_{\beta\alpha}(\mathbf{k}, \bar{\mathbf{k}}_0) \frac{1}{(2\pi)^2} \frac{1}{\bar{q}_0} \tilde{L}(q + \bar{q}_0; \mathbf{k} - \bar{\mathbf{k}}_0), \quad (3.11)$$

which corresponds to the mean intensity for incident plane waves. In general, the computation cannot be made more explicit. When the covariance function is radial, that is  $C(\mathbf{r}) =: C(r)$ , the Fourier transform  $\tilde{L}(q; \mathbf{k}) = \tilde{L}(q; k)$  reduces to a single integral that can easily be evaluated numerically:

$$\tilde{L}(q; k) = 2\pi \int_0^\infty [L(q; r) - e^{-q^2 C(0)}] r J_0(kr) dr + 4\pi^2 e^{-q^2 C(0)} \delta(\mathbf{k}) \quad (3.12)$$

where  $J_0$  is the Bessel function. For numerical purposes, the Fourier integral has been split into a convergent part and a delta function located at zero. In the case of Gaussian covariance

$$C(\mathbf{r}) =: C(r) = \sigma^2 \exp(-r^2/\xi^2), \quad (3.13)$$

a simple analytic expression can be obtained in the high-frequency limit, the so-called geometrical optics (GO) approximation. Here  $\sigma$  is the RMS height and  $\xi$  is the correlation length. For  $r \ll \xi$  we have  $L(q; r) \simeq \exp(-\frac{q^2 r^2 s^2}{2})$ , while for  $r \gg \xi$  we have  $L(q; r) \simeq \exp(-q^2 \sigma^2)$ . Noting that each asymptotic form is preponderant with respect to the other in the respective domains, we may approximate

$$L(q; r) = \exp\left(-\frac{q^2 r^2 s^2}{2}\right) + \exp(-q^2 \sigma^2), \quad (3.14)$$

and thus

$$\tilde{L}(q; k) = \frac{2\pi}{s^2 q^2} \exp\left(-\frac{k^2}{2q^2 s^2}\right) + \exp(-q^2 \sigma^2) \delta(\mathbf{k}).$$

This implies

$$\langle I_{\beta\alpha}(\mathbf{k}, \bar{\mathbf{k}}_0) \rangle = A_{\beta\alpha}(\mathbf{k}, \bar{\mathbf{k}}_0) \frac{1}{2\pi \bar{q}_0 (q + \bar{q}_0)^2 s^2} \exp\left(-\frac{|\mathbf{k} - \bar{\mathbf{k}}_0|^2}{2s^2 (q + \bar{q}_0)^2}\right) + K \bar{q}_0 e^{-4(\bar{q}_0 \sigma)^2} \delta(\mathbf{k}), \quad (3.15)$$

where we have introduced the RMS slope  $s = \sqrt{2}\sigma/\xi$ .

The same expression has been obtained in [7] (p 127) by a stationary phase argument. Note that the error in the approximation (3.14) is of the order of  $\exp(-q^2 \sigma)$ . Hence, the

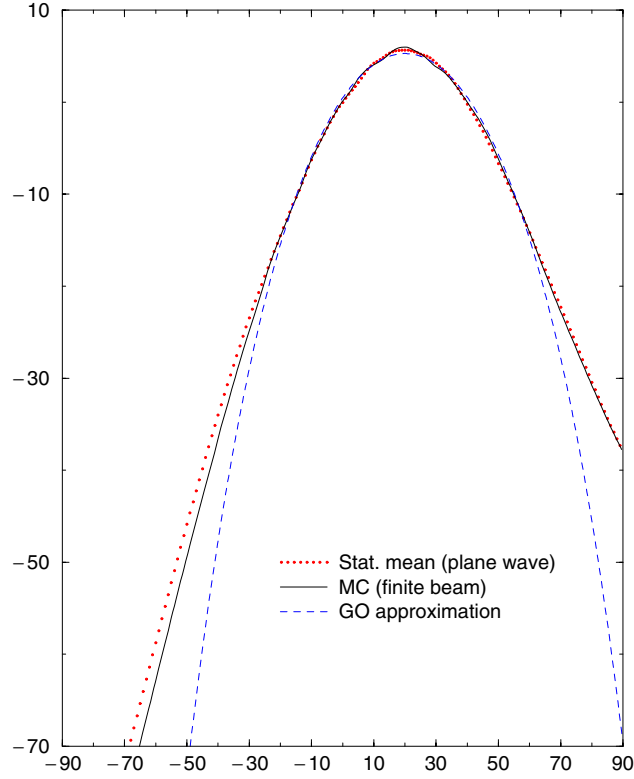


**Figure 4.** Scattering pattern in the KA for incident plane waves (statistical result), dotted curve, and Gaussian beams (Monte Carlo), solid curve.

expression (3.15) for the scattering amplitude under the KA or SSA becomes accurate for a large Rayleigh parameter  $q\sigma$ , that is for large roughness, as long as one remains in the domain of validity of the corresponding approximation.

Figure 4 shows the comparison of  $10 \log I_{11}$  in the mean plane of incidence for varying  $\theta$ , for a surface with Gaussian correlation,  $l_x = l_y = 4\lambda$ ,  $\sigma = 0.25$  and  $\xi = 3.15$ . The first curve is obtained after (3.12), the second is obtained by Monte Carlo simulation on (3.10) with 1000 realizations and the third curve is the GO limit. As can be seen, the ‘finite beam’ effect for this size of spot becomes sensible only at backward grazing angles.

## 4. Method of moments

### 4.1. Formulation

The MoM is based on a surface integral representation of the scattering problem [12]. Assume the surface  $\Sigma$  is twice continuously differentiable and let  $\mathbf{n}$  be the unit normal vector directed toward the vacuum. Let  $\mathbf{E}^t = \mathbf{E}^0 + \mathbf{E}$  and  $\mathbf{H}^t = \mathbf{H}^0 + \mathbf{H}$  be the total electric and magnetic field, respectively, and  $G_{\mathbf{R}, \mathbf{R}'} = -\exp(iK_0 |\mathbf{R} - \mathbf{R}'|) / 4\pi |\mathbf{R} - \mathbf{R}'|$  the free-space Green function in the vacuum, where  $|\mathbf{R} - \mathbf{R}'|$  denotes the distance between the two points  $\mathbf{R}, \mathbf{R}'$ .

For a perfectly conducting material one has the boundary condition  $[\mathbf{n} \times \mathbf{E}^t]_{\Sigma} = \mathbf{0}$  on the surface and  $\mathbf{j} = [\mathbf{n} \times \mathbf{H}^t]_{\Sigma}$  is the solution of the magnetic field integral equation (MFIE) [13]:

$$\left(\frac{1}{2} + M\right)\mathbf{j} = \mathbf{n} \times \mathbf{H}^0. \quad (4.16)$$

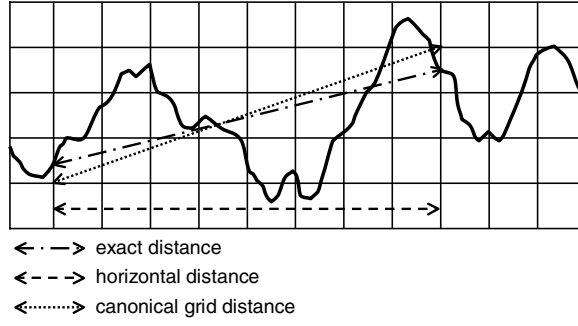


Figure 5. Canonical grid.

Here  $M$  is the integral operator introduced by Martin and Ola in [14]:

$$Mj_R = n_R \times \text{curl}_R \int_{\Sigma} G_{R,R'} j_{R'} d\Sigma',$$

where  $R = r + h(r)$  and  $R' = r' + h(r')$  are two points on  $\Sigma$ . Once the MFIE (4.16) is solved, we can deduce from the surface current  $j$  the scattered field  $E = E^t - E^0$  at a point  $R = r + z z$  of vacuum,

$$E_R = -i \frac{Z_0}{K} \text{curl}_R \text{curl}_R \int_{\Sigma} G_{R,R'} j_{R'} d\Sigma'$$

and the scattering amplitude in the direction  $K = k + qz$

$$\overline{S_{\alpha\beta}}(k, \overline{k_0}) = -\frac{Z_0}{2K} p_{\beta}(k) \cdot \int_{\Sigma} j_R \exp(-ik \cdot r - iqh(r)) d\Sigma.$$

Following [8], the MoM is applied to the MFIE (4.16) on a regular 2D grid of the  $(xOy)$  plane. The linear system associated with a bi-dimensional surface scattering problem is of large order, and its matrix  $\mathcal{M}$  is full (i.e. non-sparse). So loading this matrix in central memory would require a huge memory size, and a direct solving would need prohibitive computing time. We solve this system in an iterative way by the generalized minimum residual algorithm (GMRES) [15]. The convergence rate of this method is greatly speeded up by the use of the sparse-matrix flat-surface iterative approach [16], seen as an iterative preconditioner of the GMRES [17].

The elements of the matrix  $\mathcal{M}$  are distributed into two matrices  $\mathcal{S}$  and  $\mathcal{W}$ , using a neighbourhood distance  $r_d$ . The elements corresponding to an interaction at a horizontal distance  $|r - r'|$  (see figure 5) smaller than this neighbourhood distance  $r_d$  constitute the *strong* matrix  $\mathcal{S}$ , the other elements belong to the *weak* matrix  $\mathcal{W}$ :

$$\mathcal{M} = \mathcal{S} + \mathcal{W} : \begin{cases} |r - r'|_{ij} \leq r_d \Rightarrow \mathcal{S}_{ij} = \mathcal{M}_{ij}, & \mathcal{W}_{ij} = 0 \\ |r - r'|_{ij} > r_d \Rightarrow \mathcal{S}_{ij} = 0, & \mathcal{W}_{ij} = \mathcal{M}_{ij}. \end{cases}$$

The neighbourhood distance  $r_d$  is chosen on physical and numerical criteria, so that the strong matrix  $\mathcal{S}$  is a sparse matrix, whose non-zero elements can be loaded in central memory. The elements of the weak matrix  $\mathcal{W}$  are recomputed for each use. Three wavelengths is a typical value for the neighbourhood distance  $r_d$ .

Due to the short-range coupling effect, the strong matrix contains the most important interactions. We take it as the first approximation of the system matrix  $\mathcal{M}$ , so its inverse can be used as a preconditioning matrix for the GMRES:  $\mathcal{P} = \mathcal{S}^{-1}$ . When the neighbourhood

distance  $r_d$  is large compared with  $K\sigma^2$ , the far interactions can be approximated by the flat-surface matrix  $\mathcal{F}$ . The flat-surface matrix elements are obtained by substituting the horizontal distance  $|\mathbf{r} - \mathbf{r}'|$  for the exact distance  $|\mathbf{R} - \mathbf{R}'|$  in the Green function expression. Elements corresponding to neighbour points ( $|\mathbf{r} - \mathbf{r}'| < r_d$ ) are set to zero:

$$\mathcal{F} : \begin{cases} |\mathbf{r} - \mathbf{r}'|_{ij} \leq r_d \Rightarrow \mathcal{F}_{ij} = 0 \\ |\mathbf{r} - \mathbf{r}'|_{ij} > r_d \Rightarrow \mathcal{F}_{ij} = \mathcal{M}_{ij} (|\mathbf{R} - \mathbf{R}'| \leftarrow |\mathbf{r} - \mathbf{r}'|). \end{cases}$$

As the  $(xOy)$  plane is regularly gridded, the flat-surface matrix  $\mathcal{F}$  can be written as a combination of 2D Toeplitz matrices. Such matrices are submatrices of 2D circulant matrices, which are diagonal in the Fourier space. 2D Toeplitz matrices can so be loaded in central memory, and the matrix–vector product can be quickly performed by 2D fast-Fourier transforms. When using the flat-surface matrix, the preconditioning matrix is the inverse of the sum of the strong and the flat-surface matrix:  $\mathcal{P} = (\mathcal{S} + \mathcal{F})^{-1}$ .

These expressions of the preconditioning matrix  $\mathcal{P}$  are only formal, as the inverse matrices  $\mathcal{S}^{-1}$  and  $(\mathcal{S} + \mathcal{F})^{-1}$  are unknown to us. Practically, the product  $\mathbf{Y}$  of a given vector  $\mathbf{X}$  by the preconditioning matrix  $\mathcal{P}$  is realized by solving the linear system  $\mathbf{X} = \mathcal{P}^{-1} \mathbf{Y}$ , i.e.  $\mathbf{X} = \mathcal{S} \mathbf{Y}$  or  $(\mathcal{S} + \mathcal{F}) \mathbf{Y}$ . Thanks to the properties of the matrices  $\mathcal{S}$  and  $\mathcal{F}$ , these systems are quickly solved in an iterative way. For this, we use the biconjugate gradient stabilized algorithm.

Such a preconditioned GMRES converges typically in ten iterations, depending on the roughness of the surface.

#### 4.2. The 3D canonical grid technique

The most time-consuming operation of this MoM is the computing of  $\mathcal{W}$  and its product by a vector. To overcome this problem, we have implemented the multilevel expansion [18] of the canonical grid method [19]. The  $z$ -axis is discretized to insert the surface region into a regularly spaced 3D grid. The far interactions are computed through a Taylor series expansion of the Green function about the nodes of the 3D grid. Each term of this series is a combination of 3D Toeplitz matrices, which can be handled in the same way as previously, with 3D fast-Fourier transform.

For the present study, we have only considered the first term of the Taylor series expansion. For any two points, the canonical grid distance (see figure 5) is defined as the distance between the nearest points on the 3D grid.

This canonical grid distance is used in the expression of the elements of the matrix  $\mathcal{W}$  instead of the exact distance. A precise computation requires a tight sampling of the  $z$ -axis. Our results have been validated by a convergence test. When the  $z$ -axis sampling step decreases, the scattered intensity pattern computed with the 3D canonical grid tends to the pattern computed with the exact Green function. The 3D canonical grid technique is particularly efficient for mildly rough surfaces, where the necessary number of sampling points on the  $z$ -axis is small, typically 8, 16 or 32.

#### 4.3. Beam decomposition and parallel computations

Even with such an advanced MoM, there is a maximum surface area that can be handled with given numerical facilities: in order to be efficient, our algorithm needs the strong matrix to be stored in random access memory, and the size of this matrix increases linearly with the surface area. Moreover, a large surface takes prohibitive computing time. In a Monte Carlo simulation, this maximum size may be too small to represent the statistical properties of a random rough surface. Beam decomposition is an elegant way to overcome this difficulty. It was originally developed for one-dimensional random rough surfaces [20], but adaptation to two-dimensional surfaces is straightforward [17]. Beam decomposition is based on the

**Table 1.** Surfaces parameters for Gaussian correlation functions.

Surface	RMS height	Correl. length	RMS slope	Figure
1	0.25	3.15	0.112(6.4°)	
2	0.05	0.63	0.112(6.4°)	
3	0.5	3	0.24(13.3°)	6
4	0.25	1.5	0.24(13.3°)	
5	0.167	1	0.24(13.3°)	7
6	0.125	0.75	0.24(13.3°)	
7	0.083	0.5	0.24(13.3°)	8
8	0.5	2	0.35(19.5°)	9
9	0.5	1.5	0.47(25.2°)	
10	0.25	0.75	0.47(25.2°)	
11	1	2	0.71(35.3°)	

representation of a *large* beam as a weighted sum of shifted *narrow* beams. Each narrow beam is handled as a particular scattering problem. Summing the scattering amplitudes  $\overline{S_{\alpha\beta}^{ij}}$  of all the narrow beams provides the scattering amplitude of the large one  $\overline{S_{\alpha\beta}}$ .

Following section 2.2, the incident large beam is characterized by dimensions  $\ell_x$  and  $\ell_y$ . In a similar way, the incident narrow beams have dimensions  $n_x < \ell_x$  and  $n_y < \ell_y$ . For the scattering amplitude,

$$\overline{S_{\alpha\beta}}(\mathbf{k}, \mathbf{k}_0) = \sum_{i=-N_x}^{N_x} \sum_{j=-N_y}^{N_y} u_{ij}(\mathbf{k} - \mathbf{k}_0^m) \overline{S_{\alpha\beta}^{ij}}(\mathbf{k}, \mathbf{k}_0)$$

where  $\mathbf{r}_{ij} = (i \Delta X, j \Delta Y)$  and

$$u_{ij}(\mathbf{k}) = \frac{\Delta X \Delta Y}{2\pi} \frac{\exp(-i\mathbf{k} \cdot \mathbf{r}_{ij})}{\sqrt{\ell_x^2 - n_x^2} \sqrt{\ell_y^2 - n_y^2}} \exp -\frac{1}{2} \left( \frac{(i\Delta X)^2}{\ell_x^2 - n_x^2} + \frac{(j\Delta Y)^2}{\ell_y^2 - n_y^2} \right).$$

Numerical experimentation has shown that a good representation of the large beam is achieved as soon as  $\Delta X \simeq 2n_x$  and  $\Delta Y \simeq 2n_y$ .

The beam decomposition is naturally well fitted for parallel computation. As a matter of fact, after the rough surface is divided and weights for the decomposition are evaluated, the following tasks (computation of the incident field on the surface, building the matrices, solving the system and computing the scattering amplitude) can be performed independently for each narrow beam. Then, scattering amplitudes only need be summed. This scheme is particularly adapted to distributed memory parallel environment.

## 5. Numerical results

### 5.1. Single-scale surfaces

For our first experiment, we have chosen the prototype of single-scale surfaces, namely surfaces with Gaussian correlation function (3.13). These are parametrized only by the RMS height  $\sigma$  and the correlation length  $\xi$ . An additional parameter for the validity of the approximations is the RMS slope  $s = \sqrt{2}\sigma/\xi$ . We have been working on surfaces numbered from 1 to 11, whose parameters are summarized in table 1. Here and everywhere, the unit of length is the electromagnetic wavelength. The minimum value 0.5 of the correlation length is imposed by the numerical limitations of the MoM: for memory storage and computation time considerations, the maximum sampling rate of the surface has been set to 64 points per square wavelength.

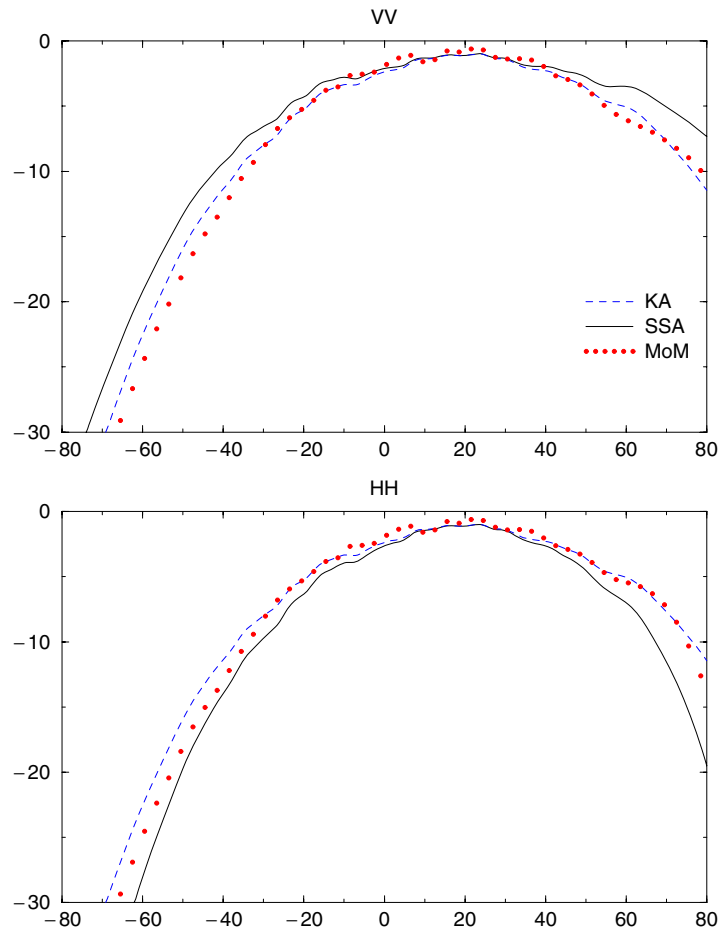


Figure 6. Surface 3.

### 5.2. Scattering diagrams

Figures 6–9 compare the co-polarized scattered intensity in the incidence plane according to the MoM, KA and SSA for some representative surfaces (3, 5, 7, 8). We have performed a Monte Carlo simulation over 500 sample surfaces for the approximate methods (computed after (3.10)) and over at least 100 sample surfaces for the MoM. The intensity has been given in decibels, that is  $10 \times \log(\text{intensity})$  has been plotted.

Surface 2 falls into the usually acknowledged limit of the SPM domain. The SSA is accurate over the whole scattering diagram while the KA is irrelevant outside the specular region. This is natural since the SSA is designed to meet the SPM at small roughness. As one increases the RMS height to leave the domain of validity of the SPM (surface 7), the SSA is still better than the KA and is accurate in the forward direction but starts deteriorating in the backward direction. Increasing the correlation length while keeping the slope constant ( $=13.3^\circ$ ), we observe a continuous transition from the SSA to the KA (surfaces 6, 5, 4, 3) as the most accurate method, the turning point being surface 5. For higher values of the RMS slope (surfaces 8–11), the SSA is never reliable while the KA remains good up to RMS slope value of  $19.5^\circ$  for large correlation length (surface 8). Note that for large correlation length,

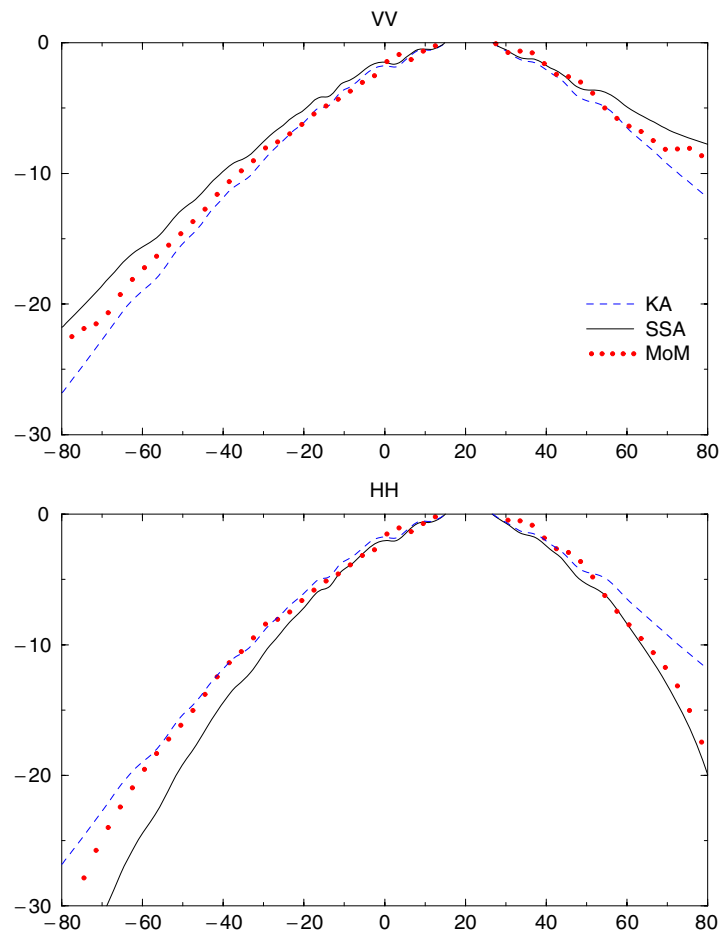


Figure 7. Surface 5.

the SSA is accurate only for very small values of the slope (surface 1). Judging from this sample of surface statistics, one can conclude that the RMS slope is not the only relevant parameter for the accuracy of the SSA, which is in fact also very sensitive to the value of the RMS height. For a given (reasonably small) slope, the SSA becomes truly reliable only for smaller values of the RMS height but one has to resort to the KA for larger RMS. The SSA domain is often qualitatively depicted by the area below a hyperbola in the usual  $1/\xi, \sigma$  diagram (see e.g. [7, p 4]) and is often assumed to cover both the KA and the SPM domain. For the first-order SSA, the validity domain is more intricate. We suggest a refined diagram based on the few available surface types, see figure 10. An important fact to note is that the SSA, at least at first order, does not truly bridge the gap between the KA and the SPM since it fails to cover the large correlation length part of the KA domain. The second-order SSA seems very promising in that respect but more difficult to implement; it will be tested subsequently. Thus the KA and the SSA play complementary roles, as far as first-order approximations are concerned. Note, however, that we have only considered the case of small incidence ( $20^\circ$ ), which favours the KA. The above conclusions would not necessarily hold at grazing incidences.

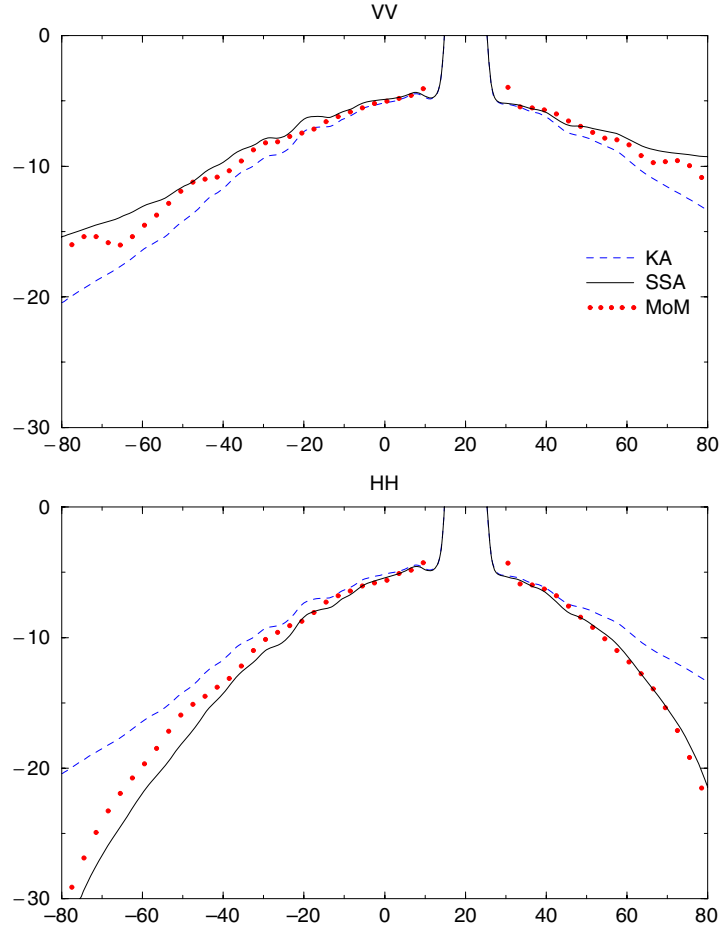
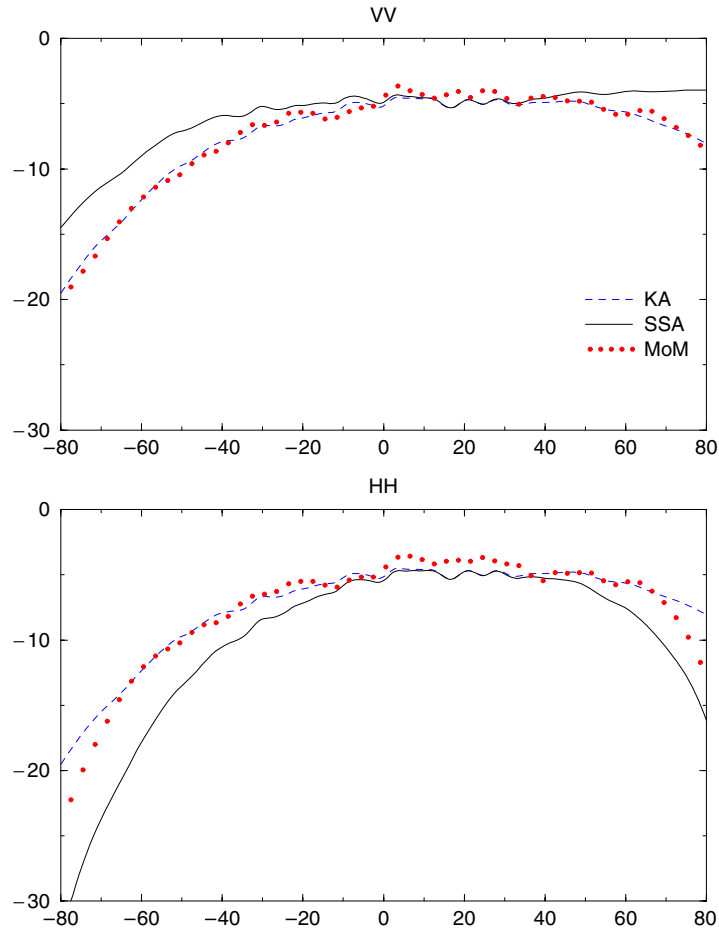


Figure 8. Surface 7.

Since most active remote sensing techniques are concerned with the backscattering cross section, special attention has been devoted to it. We have computed the exact and approximated backscattering coefficient for surfaces 1–9. To get rid of the remaining Monte Carlo fluctuations, a  $10^\circ$  angular average has been performed around the backscattering direction for each method. Table 2 summarizes the numerical results. Column 1 gives the surface and polarization, column 2 is the exact co-polarized backscattering coefficient  $\sigma_{\text{co}}^{\text{MoM}} = 10 \log I_{\alpha\alpha}$ , given in dB, columns 3 and 4 give the KA co-polarized backscattering coefficient  $\sigma_{\text{co}}^{\text{KA}}$  and the relative deviation  $\Delta\sigma_{\text{co}}^{\text{KA}} = (\sigma_{\text{co}}^{\text{KA}} - \sigma_{\text{co}}^{\text{MoM}})/\sigma_{\text{co}}^{\text{MoM}}$  to the MoM, respectively; columns 5 and 6 are similar for the SSA and column 7 is the polarization ratio  $\rho^{\text{MoM}} = I_{\text{VV}}^{\text{MoM}}/I_{\text{HH}}^{\text{MoM}}$ . As was noted before on the scattering diagrams, the KA is generally more accurate than the SSA outside the near-perturbative domain (that is surfaces 2 and 7) and no further away than 10% from the exact value, in both polarizations. Note that, surprisingly, the KA is less accurate for surface 1 than surface 3 which has almost the same correlation length but twice the RMS height. This is due to the lack of precision of the MoM in the diffuse part for shallow rough surfaces.

Another interesting parameter is the polarization ratio  $\rho^{\text{MoM}}$ . As can be seen in table 2, it strongly depends on the surface roughness, a sensibility that is not captured by either



**Figure 9.** Surface 8.

approximation. Indeed,  $\rho^{\text{KA}} = 1$  and  $\rho^{\text{SSA}} = (1 + \sin^2 \bar{\theta}_0)^2 \cos^{-4} \bar{\theta}_0 = 1.6$  as can be seen by an easy calculation using (3.8). Note, however, that  $\rho^{\text{KA}}$  remains within 10% of  $\rho^{\text{MoM}}$  except for surfaces 2 and 7, whereas  $\rho^{\text{SSA}}$  overestimates by far the polarization ratio.

*5.2.1. Energy balance.* We have computed the energy balance (in per cent) for the different approximations and polarization cases. Figure 11 shows the isolines in the usual RMS height versus inverse correlation length diagrams. As expected, the energy balance of the KA improves for increasing correlation length and decreasing RMS height; for large values of the Rayleigh parameter, the isolines are hyperbolae as predicted by the GO approximation (3.15). In fact, the hyperbolic behaviour can be observed on the whole diagram. The energy diagrams are more complex for the SSA. In the region with large correlation radius, the isolines are no longer hyperbolic and the energy balance is slightly overestimated, for both polarizations. Furthermore, the 100% isoline passes through a region where the SSA has been shown to be irrelevant in the previous section (surface 9). Thus the energy balance criterion cannot be considered as a reliable test of accuracy for the method in that case. Note that there is no qualitative difference between the two polarizations for the SSA. However, this is not true in

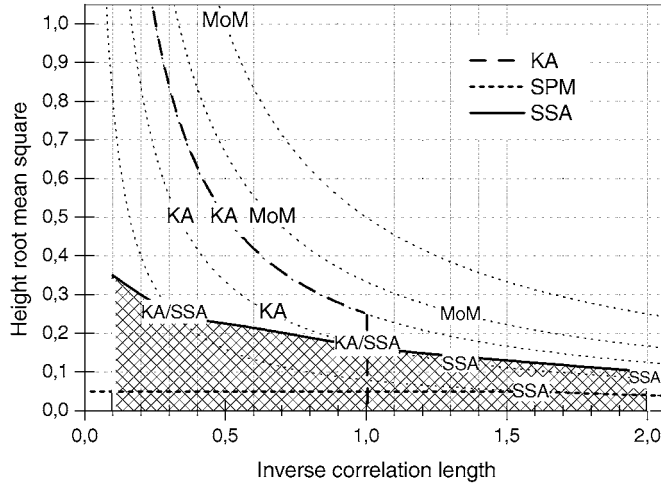


Figure 10. Validity domain of the approximations.

Table 2. Backscattering properties for Gaussian surfaces.

N	$\sigma_{co}^{MoM}$	$\sigma_{co}^{KA}$	$\Delta\sigma_{co}^{KA}\%$	$\sigma_{co}^{SSA}$	$\Delta\sigma_{co}^{SSA}$	$\rho^{MoM}$
1V	-15.7	-14.9	-4.7	-14	-10.9	
1H	-16.2	-14.9	-7.71	-16	-1.09	1.10
2V	-10.8	-11.4	5.67	-10.4	-3.67	
2H	-12.5	-11.4	-9.2	-12.4	-0.614	1.50
3V	-5.09	-5.23	2.8	-4.2	-17.4	
3H	-5.23	-5.23	-0	-6.38	22.1	1.03
4V	-5.53	-5.69	2.86	-4.81	-12.9	
4H	-5.85	-5.69	-2.8	-6.78	15.9	1.07
5V	-6.2	-6.02	-2.86	-5.09	-17.9	
5H	-6.58	-6.02	-8.44	-7.21	9.68	1.12
6V	-6.58	-6.58	-0	-5.69	-13.5	
6H	-7.21	-6.58	-8.83	-7.7	6.7	1.13
7V	-7.45	-7.7	3.33	-6.78	-8.99	
7H	-8.54	-7.7	-9.88	-8.86	3.77	1.33
8V	-5.85	-6.2	5.94	-5.09	-13.1	
8H	-5.53	-6.2	12.1	-7.21	30.5	0.96
9V	-6.02	-7.45	23.7	-6.38	6.01	
9H	-5.38	-7.45	38.5	-8.54	58.8	0.88
10V	-6.99	-7.21	3.19	-6.2	-11.3	
10H	-6.38	-7.21	13	-8.24	29.1	0.90
11V	-6.2	-10.2	64.2	-9.21	48.6	
11H	-5.23	-10.2	94.6	-11.3	116	0.80

the 1D case, where a strange phenomenon appears in V-polarization: the energy balance is largely overestimated over the whole diagram. This anomaly has not been reported previously in the literature, to our knowledge. In fact, we are only aware of 1D numerical simulations in H-polarization for the SSA [2, 21]. Hence, there may be some pitfalls in extrapolating 2D results from 1D studies.

The energy balance has also been checked for the MoM. For slopes up to  $13.3^\circ$  (surfaces 1–7), the error is less than 1%. For higher slopes, the energy balance deteriorates



**Table 3.** Backscattering properties for ocean-spectra.

	MoM	KA	SSA
$\sigma_{VV}$	$3.01 \times 10^{-2}$	$2.73 \times 10^{-2}$	$3.40 \times 10^{-2}$
$\sigma_{HH}$	$2.34 \times 10^{-2}$	$2.73 \times 10^{-2}$	$2.13 \times 10^{-2}$
$\rho$	1.29	1	1.6
$\Delta\Phi$	0	0.6%	0.8%

of the low-frequency cutoff is imposed by the numerical limitations:  $\kappa_l = K/30$ , where  $K$  is the electromagnetic wavenumber, which corresponds to a maximum scale of  $30\lambda$ . Note that a true  $\kappa^{-4}$  surface is not differentiable. However, the spectrum decays fast enough to ensure that high-frequencies do not contribute to the scattering process. We have set  $\kappa_u = 4K$ , which has been shown numerically in the 1D case to be the electromagnetic cutoff. The multiplicative factor has been set to  $\alpha = 5.25 \times 10^{-3}$  in order to fit the Elfouhaily spectrum in the considered range of frequency for L-band wavelength ( $\lambda = 20$  cm). A remarkable feature of the truncated  $\kappa^{-4}$  spectra is that neither  $K\sigma$  nor  $s$  depends on the value of the wavelength. Indeed, a simple computation of the zeroth and second moments of the spectrum yields

$$K\sigma = \sqrt{\frac{\alpha}{2}} \sqrt{\left(\frac{\kappa_l}{K}\right)^{-2} - \left(\frac{\kappa_u}{K}\right)^{-2}} = 1.537 \quad (5.19)$$

$$s = \sqrt{\alpha \ln(\kappa_u/\kappa_l)} = 0.112. \quad (5.20)$$

Hence, even though the spectrum (5.17) has been designed to fit realistic sea spectra, the results we derive are universal, in the sense that they do not depend on the value of the wavelength.

The KA is *a priori* not adapted to multi-scale surfaces, which are not smooth. Also, the RMS height of the considered surface is well beyond the usual SPM domain ( $k\sigma < 0.3$ ). The small value of the slope, however, makes the SSA a good candidate. Figures 12 and 13 show Monte Carlo simulations of the scattering intensity for the KA, the SSA, the SPM and the MoM. The ensemble average has been performed over 1000 sample surfaces for the approximate methods and 100 sample surfaces (due to the huge computational time) for the MoM. Both the KA and the SSA turn out to be extremely accurate (less than 0.5 dB error) in both polarizations for small angles ( $-30^\circ \leq \theta \leq +50^\circ$ ), but only the SSA remains reliable over the whole range of scattering angles (less than 1 dB error in VV and for  $-65^\circ \leq \theta \leq +75^\circ$  in HH). The SPM overestimates by far the scattering coefficient in the specular region but becomes reliable at larger angles as it meets the SSA. The values of the backscattering intensity are given in table 3, as well as the polarization ratio  $\rho$  and the energy balance. The error on the latter quantities are equivalent for both approximations and polarizations.

Note that the KA and the SSA coincide in the specular direction and remain extremely close to one another (within 0.5 dB) up to the backscattering direction. This is due to the small value of the incidence angle ( $\bar{\theta}_0 = 20^\circ$ ). We expect a more highly contrasted backscattering intensity in favour of the SSA for larger incidences (for instance, the backscattering coefficient differs by more than 2 dB at  $30^\circ$ ).

Hence, the SSA is well adapted and more accurate than the KA for ocean-like spectra in the considered frequency band (even though both approximations have comparable performances in the backscattering direction, due to the small incidence angle). Note that the opposite conclusion was drawn on the Gaussian single-scale surface (surface 1) with the same first spectral moments (5.19) and (5.20). This confirms that the RMS slope is not the only relevant parameter for the validity of the SSA, which is also sensitive to the kind of spectrum.

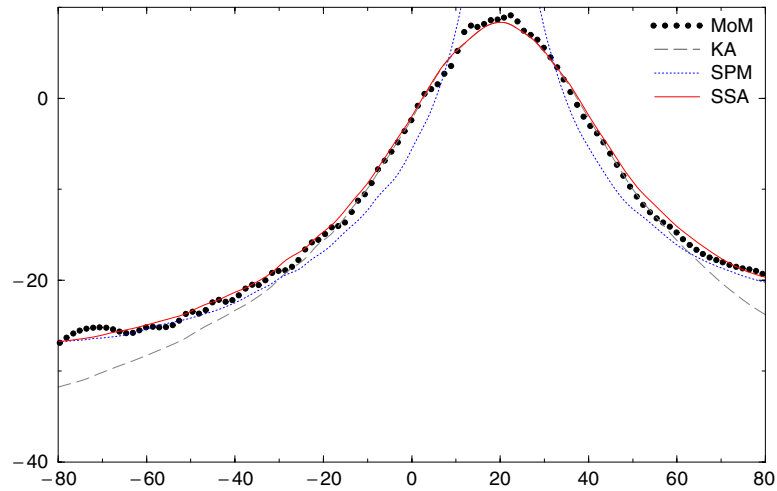


Figure 12. V copolarization. Comparison of MoM, KA and SSA for a sea surface VV.

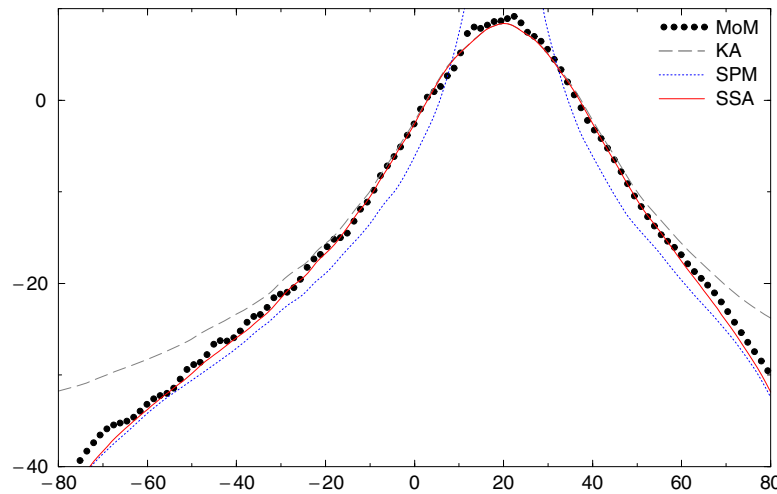


Figure 13. H copolarization. Comparison of MoM, KA and SSA for a sea surface HH.

## 6. Conclusion

In this paper, we have compared numerically the accuracy of the KA and the SSA for two representative types of rough surfaces. For single-scale (Gaussian) surfaces, the SSA at first order is disappointing outside the near-perturbative domain, even for small slopes, as in many respects it is outperformed by the KA. Furthermore, the energy balance is not reliable as an accuracy criterion, unlike the KA. However, when it comes to (band-limited) ocean-like surfaces, the SSA performs better than the KA, and for RMS height and slope values where the converse holds in the case of Gaussian correlations. This shows that the RMS slope is not the sole relevant parameter for the accuracy of the SSA, which turns out to be strongly dependent on the type of spectrum. Thus, the SSA appears to be the better adapted first-order approximate method for ocean-like surfaces, provided that a low spatial frequency cutoff is used. This suggests an improve-

ment of the usual two-scale model, by replacing the SPM by the SSA in the high-frequency part of the spectrum. In this way, the cutoff wavenumber could be shifted down to larger frequencies (in our case  $K/30$ ) that fall plainly in the Kirchhoff domain. This is left for further research.

## References

- [1] Ogilvy J A 1991 *Theory of Wave Scattering from Random Rough Surfaces* (Bristol: Adam Hilger)
- [2] Thorsos E I and Broschat S L 1997 An investigation of the small-slope approximation for scattering from rough surfaces. part II. Numerical studies *Waves Random Media* **101** 2615–25
- [3] McDaniel S T 1999 Acoustic and radar scattering from directional seas *Waves Random Media* **9** 537–49
- [4] Johnson J T 1998 A numerical study of the composite surface model for ocean backscattering *IEEE Geosci. Remote Sens.* **36** 72–83
- [5] Voronovitch A G 1985 Small-slope approximation in wave scattering from rough surfaces *Sov. Phys.–JETP* **62** 65–70
- [6] Voronovitch A G 1994 Small-slope approximation for electromagnetic wave scattering at a rough interface of two dielectric half-spaces *Waves Random Media* **4** 337–67
- [7] Voronovitch A G 1994 *Wave Scattering from Rough Surfaces (Springer Series on Wave Phenomena)* (Berlin: Springer)
- [8] Pak K, Tsang L, Chan C H and Johnson J T 1995 Backscattering enhancement of electromagnetic waves from two-dimensional perfectly conducting random rough surfaces based on Monte Carlo simulations *J. Opt. Soc. Am. A* **12** 1491–9
- [9] Tran P and Maradudin A A 1994 The scattering of electromagnetic waves from a randomly rough 2D metallic surface *Opt. Commun.* **110** 269–73
- [10] Song J M and Chew W C 1995 Moment method solutions using parametric geometry *J. Electromagn. Waves Appl.* **9** 71–83
- [11] Braunsch H, Zhang Y, Ao C O, Shih S E, Yang Y E, Ding K H and Kong J A 2000 Tapered wave with dominant polarization stat for all angles of incidence *IEEE Trans. Antennas Propag.* **48** 1086–96
- [12] Wang J J H 1991 *Generalized Moment Method in Electromagnetics* (New York: Wiley-Interscience)
- [13] Colton D and Kress R 1983 *Integral Equations in Scattering Theory* (New York: Wiley-Interscience)
- [14] Martin P A and Ola P 1993 Boundary integral equations for the scattering of electromagnetic waves by a homogeneous dielectric obstacle *Proc. R. Soc. Edinburgh A* **123** 185–208
- [15] Saad Y 1996 *Iterative Methods for Sparse Linear Systems* (New York: PWS)
- [16] Johnson J T, Tsang L, Shin R T, Pak K, Chan C H, Ishimaru A and Kuga Y 1996 Backscattering enhancement of electromagnetic waves from two-dimensional perfectly conducting random rough surfaces: a comparison of Monte Carlo Simulations with experimental data *IEEE Trans. Antennas Propag.* **44** 748–56
- [17] Soriano G and Saillard M 2001 Scattering of electromagnetic waves from two-dimensional rough surfaces with impedance approximation *J. Opt. Soc. Am. A* **18** 124–33
- [18] Li S-Q, Chan C H, Xia M-Y, Zhang B and Tsang L 2001 Multilevel expansion of the sparse-matrix canonical grid method for two-dimensional random rough surfaces *IEEE Trans. Antennas Propag.* **47** 752–63
- [19] Pak K, Tsang L and Johnson J T 1997 Numerical simulations and backscattering enhancement of electromagnetic waves from two-dimensional dielectric random rough surfaces with the sparse canonical grid method *J. Opt. Soc. Am. A* **14** 1515–29
- [20] Saillard M and Maystre D 1988 Scattering from random rough surfaces: a beam simulation method *J. Opt.* **19** 173–6
- [21] Broschat S L 1993 The small slope approximation reflection coefficient for scattering from a Pierson–Moskowitz sea surface *IEEE Trans. Geosci. Remote Sens.* **31** 1112–14
- [22] Franceschetti G, Iodice A, Migliaccio M and Riccio D 1999 Scattering from natural rough surfaces modeled by fractional Brownian motion *IEEE Trans. Antennas Propag.* **47** 1405–15
- [23] Guérin C A and Saillard M 2001 Inverse scattering on fractional Brownian surfaces and estimation of the Hurst exponent *Inverse Problems* **17** 365–86
- [24] Elfouhaily T, Chapron B and Katsaros K 1997 A unified directional spectrum for long and short wind-driven waves *J. Geophys. Res.* **102** 15 781–96